



HAL
open science

Imaging the hydraulic properties of a contaminated alluvial aquifer perturbed with periodic signals

P. Fischer, T. de Clercq, Abderrahim Jardani, L. Thannberger, Nicolas Massei, M. Abbas

► **To cite this version:**

P. Fischer, T. de Clercq, Abderrahim Jardani, L. Thannberger, Nicolas Massei, et al.. Imaging the hydraulic properties of a contaminated alluvial aquifer perturbed with periodic signals. *Hydrogeology Journal*, 2020, 28, pp.2713-2726. 10.1007/s10040-020-02233-8 . insu-03661816

HAL Id: insu-03661816

<https://insu.hal.science/insu-03661816v1>

Submitted on 24 Jul 2023

HAL is a multi-disciplinary open access archive for the deposit and dissemination of scientific research documents, whether they are published or not. The documents may come from teaching and research institutions in France or abroad, or from public or private research centers.

L'archive ouverte pluridisciplinaire **HAL**, est destinée au dépôt et à la diffusion de documents scientifiques de niveau recherche, publiés ou non, émanant des établissements d'enseignement et de recherche français ou étrangers, des laboratoires publics ou privés.



Distributed under a Creative Commons Attribution - NonCommercial - NoDerivatives 4.0 International License

Imaging the hydraulic properties of a contaminated alluvial aquifer perturbed with periodic signals

P. Fischer¹, T. De Clercq^{1,2}, A. Jardani¹, L. Thannberger², N. Massei¹, M. Abbas³

(1) Normandie Univ, UNIROUEN, UNICAEN, CNRS, M2C, 76000 Rouen, France

(2) VALGO, 76650 Petit Couronne, France

(3) School of Engineering, Lebanese International University, Beirut, Lebanon

Conflict of interest: None

Corresponding author: P. Fischer

E-mail : pierre.fischer1@univ-rouen.fr

Key words: Oscillatory pumping test, Periodic signal, Inverse modeling, Characterization, France

1 **Abstract**

2 Imaging characterization of a heterogeneous alluvial aquifer at a decametric scale is presented.
3 The characterization relies on responses to oscillatory pumping tests led in two different wells
4 and at two different periods of oscillation (5 and 10 min). These specific oscillatory responses
5 are extracted from the hydraulic pressure values, measured in 13 boreholes during the pumping
6 tests, through a data processing procedure. Then, a deterministic inversion process, led with a
7 two-dimensional hydraulic properties model, aims to reproduce this set of oscillatory responses,
8 in a frequency domain, by optimizing the distribution of the property values in the model. Two
9 inversion processes are led separately with each set of responses corresponding to the two
10 periods of oscillation used, and one joint inversion is led with the set of all responses together.
11 The inversion results image the heterogeneities in the distribution of the field properties. The
12 results suggest that longer periods of oscillation (in this case 10 min) permit characterization of
13 larger areas around the pumping wells. In contrast, shorter periods (in this case 5 min) propagate
14 more readily in the conductive zones near the pump and provide less information for the less
15 conductive areas. Therefore, it appeared that performing a joint inversion, combining the
16 information carried by the responses to both periods, provided more information on the
17 heterogeneous distribution of the field properties and resulted in better constrained property
18 maps than the ones obtained from separate inversions.

19 **1. Introduction**

20 The assessment of subsurface hydraulic properties at field scale is a critical step for the selection
21 and the implementation of an effective remediation protocol for contaminated aquifers.
22 Generally, estimates of these properties (mainly transmissivity and storativity) are obtained
23 from the analysis of measured hydraulic signals in response to extraction of water from a
24 pumping well (Butler 2005; Batu 1998; Neuman and Witherspoon 1972; Le Borgne et al. 2004;
25 Li et al. 2008; Wen et al. 2010). The interpretation of pumping tests can be made with an
26 analytical model of the groundwater flow equation, with the assumption of homogeneity, to
27 deduce averaged values of these properties (Sanchez-Vila et al. 1999), or by using hydraulic
28 tomography to determine their spatial heterogeneity (Yeh and Lee 2007). Hydraulic
29 tomography has been widely explored during the last few decades to identify hydraulic features
30 of aquifers with various hydrogeological conditions (Yeh and Liu 2000; Zhu and Yeh 2005;
31 Bohling et al. 2007; Illman et al. 2009; Cardiff et al. 2009; Berg and Illman 2015; Fischer et al.
32 2017). The approach is mainly based on the implementation of an optimization code to find the
33 spatial distribution of the hydraulic properties able to reconstruct all recordings of hydraulic
34 data collected during the pumping tests.

35 Illman et al. (2010) show and underline the fact that an accurate spatial imaging of the hydraulic
36 properties is key to a better prediction of the contaminant transport in heterogeneous
37 contaminated aquifers. These predictions represent the basis for the design of protocols of
38 remediation for polluted sites. Therefore, characterizing the hydraulic properties in a
39 contaminated field site represents a specific research problem discussed in several recent
40 articles (Wagner 1992; Rasmussen et al. 2003; Berg and Illman 2013; Hochstetler et al. 2016).
41 However, use of the traditional pumping test requires an extraction of large water volumes in
42 order to generate measurable drawdowns, and this procedure results in additional costs for
43 treating or storing these quantities of polluted water.

44 Rasmussen et al. (2003) thereby elaborated a pumping-injection system, in which the pumped
45 water is stored in a tank, before being reinjected into the aquifer. This system generates an
46 oscillatory solicitation signal, with pumping rates oscillating between positive and negative
47 extrema, which induces oscillation in the groundwater pressure. Such oscillation of pressure
48 can also be generated without pumping, by movement of mass at the air-water interface in a
49 well (Guiltinan and Becker, 2015).

50 Making use of oscillatory rates, instead of constant rates, during the pumping tests, for the
51 characterization of the distribution of field properties, has attracted significant attention
52 (Lavenue and de Marsily 2001; Cardiff et al. 2013; Rabinovich et al. 2015; Zhou et al. 2016;
53 D’Oria et al. 2018). These oscillatory rates generate oscillatory responses over the hydraulic
54 level. A guideline has been proposed by Cardiff and Barrash (2015) for the implementation of
55 oscillatory pumping tests at field scale. The oscillatory responses can be easily extracted from
56 the other responses and noises in the measurements (Bakhos et al. 2014; Cardiff and Slayer
57 2016). Then, the amplitude decay and phase shift of the signal between a measurement point
58 and the pumping point permit assessment of information on the subsurface properties.

59 The efficiency of such signals has already been exploited to create an image of the property
60 distribution in a heterogeneous medium (Zhou et al. 2016, Cardiff et al. 2019), to estimate the
61 hydraulic connectivity between wells at a fractured site (Guiltinan and Becker 2015), to image
62 a conduit network in a karstic aquifer (Fischer et al. 2018), to detect leakage from a subsurface
63 formation (Sun et al. 2015), or to localize non-aqueous phase liquid (NAPL) sources and
64 monitor their spreading (Zhou and Cardiff 2017).

65 This work aims to quantitatively characterize, at a decametric scale, the subsurface properties
66 of a contaminated heterogeneous alluvial aquifer that is hydraulically influenced by a natural
67 tidal signal, complicating extraction of the observed response. Furthermore, as the site is
68 contaminated, the volume of water to be extracted for the characterization has to be limited.

69 Therefore, oscillatory pumping rates appear as an interesting alternative, thereby avoiding
70 problems caused by these two issues at the same time. Thus, two oscillatory pumping tests (led
71 with two different periods of oscillations) were performed at the study site, and the responses
72 were used with a deterministic inversion process to interpret the distributions of transmissivity,
73 storativity and diffusivity over the field site. Inversion processes are led separately with each
74 set of responses corresponding to both periods of oscillation used (5 min and 10 min), and also
75 jointly using both sets of responses together. The different interpretations made from these
76 different inversions will provide information, brought about by the responses to different
77 periods of oscillations at this scale.

78 The article begins with a presentation of the study site, the oscillatory pumping tests and the
79 data processing approach. Then, the modeling method and the inverse problem are detailed. In
80 the last section the results of the hydraulic imaging are provided and there is a discussion
81 concerning the choices involved in using oscillatory responses.

82 **2. Site and data presentation**

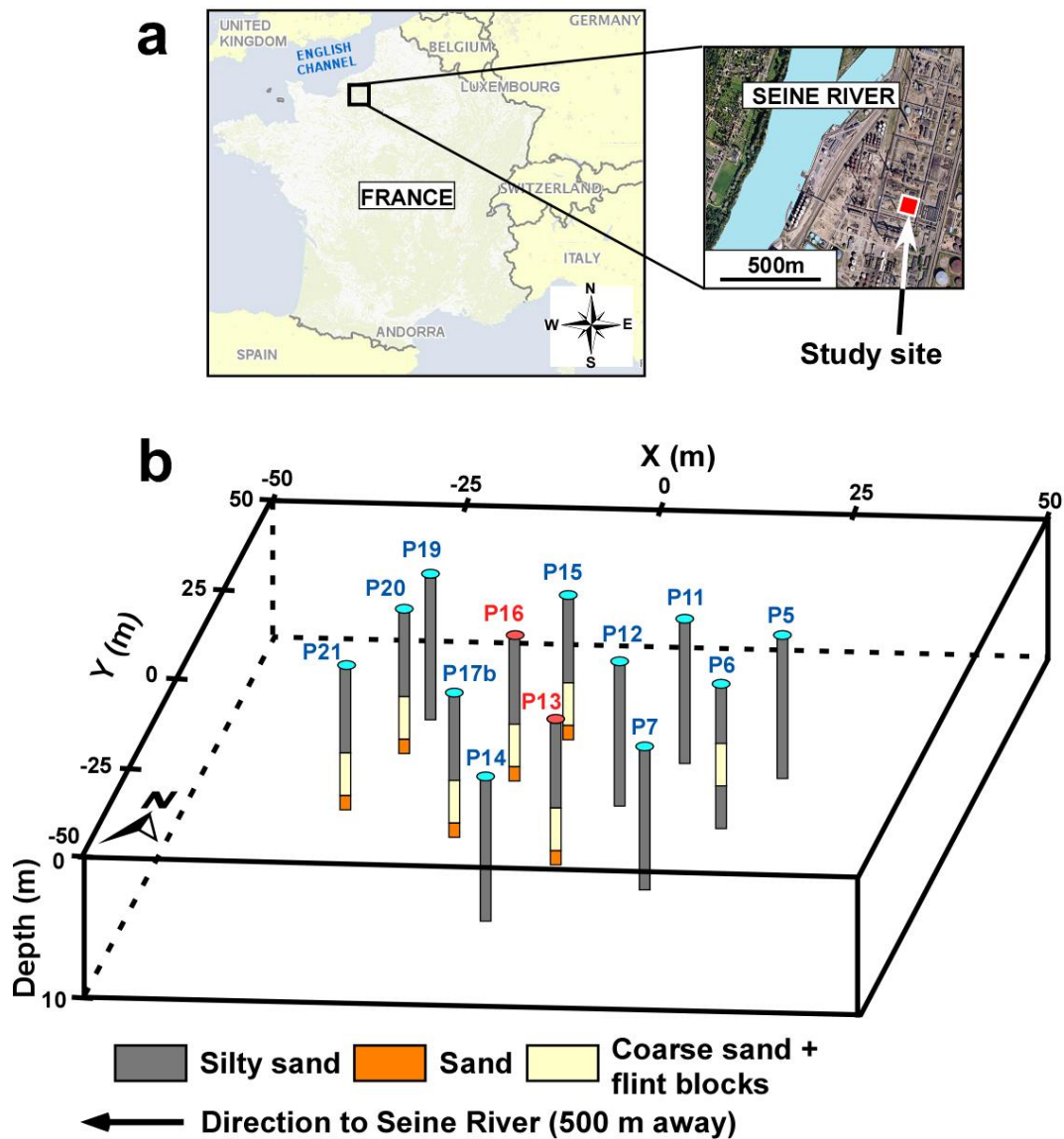
83 **2.1. Study site**

84 This work investigates the subsurface under a former petroleum refinery located near the town
85 of Rouen (Normandy), in the North West of France. The buildings of the refinery have been
86 demolished and the field site is actually in a depollution stage. The studied site corresponds to
87 a 100 m × 100 m parcel of the overall field site (see Figure 1). The subsurface of the study site
88 is composed of 10-m depth of a heterogeneous deposit (silty sands, coarse sands and chalk/flint
89 blocks) lying on a chalk horizon.

90 The investigated aquifer is limited to this heterogeneous superficial medium, wherein complex
91 flows are occurring. In order to understand the heterogeneity of this aquifer, the site is equipped
92 with 21 boreholes, drilled through the whole aquifer unit. The boreholes are made of HDPE

93 with a diameter of 163 mm and are screened from 3 m to 10 m depth. The geological logs of
94 these boreholes indicate that some wells intersect only silty sands over the 10-m thickness of
95 the aquifer, while some others intersect the same silty sand unit in the first 6 m and then a more
96 permeable unit composed of coarse sands and flint blocks from 6 m to 9 m depth (Figure 1).
97 From the logs of excavations on the wider site (near to the investigated area and showing the
98 same geological successions) and a previous hydrogeophysical study of this field site (De
99 Clercq et al., 2020), it was observed that this flint/chalk block unit can include very conductive
100 flow paths, and thus generate localized, but important, flow velocities within the site. Therefore
101 it is expected that the property distribution in this field site is highly contrasted, as this very
102 conductive unit is not spatially continuous.

103



104

105 Figure 1: a. Location of the study site in France and b. Map of location of the existing boreholes
 106 (circles) on the study site. Boreholes indicated with red circles represent the pumping wells and
 107 boreholes indicated with blue circles represent the measurement wells. The geological log of
 108 each borehole, from surface to 10-m depth, is shown on the map as a colored column.

109

110 The superficial aquifer is considered as semi-confined under the silty sands. The static water
 111 level in the aquifer is mainly influenced by the sea tidal signal of the Seine River located 500
 112 m on the west side of the study area. Floating light non-aqueous phase liquid (LNAPL) was
 113 measured with a SOLINST interface meter before pumping; two wells had significant LNAPL-

114 layer thickness prior to pumping: P19 (60 cm, i.e. 12% of the groundwater column) and P16
 115 (120 cm, i.e. 24% of the groundwater column). No floating LNAPL was present in a significant
 116 quantity in the other monitored wells of the study site during the pumping investigation.

117 The floating NAPL was regularly measured in each well of the field site between 2016 and
 118 2019. Thus, frequencies of occurrence of floating NAPL have been measured with the 30
 119 measurements performed, in each well, during this period. It is believed that this floating NAPL
 120 is more likely to be entrapped in less diffusive areas of the site. Therefore, these frequencies of
 121 occurrence were used to eventually assess the modeled spatial distribution of hydraulic
 122 diffusivity.

123 **2.2. Piezometric responses to the pumping signals**

124 Two different pumping tests were conducted in P13 and P16, each time for two different periods
 125 of oscillation of the pumping signal (5 min and 10 min). The oscillation signal was generated
 126 around a constant mean pumping signal, so that the pumps were constantly pumping, at varying
 127 rates, during the investigation. The oscillating rates were generated and piloted by an automated
 128 device, based on an electric variator, connected to the pump. This device was modified
 129 internally, as such devices are not produced for sale currently, and has been designed to control
 130 any type of pump. The different pumping tests were conducted, for each period of oscillation,
 131 long enough to produce 6 to 7 oscillations (total duration of 1 h maximum for the period of 10
 132 min). The temporal evolution of the pumping rate of these tests is given by:

$$133 \quad Q(t) = Q_{\text{mean}} - Q_{\text{amp}} \cdot \cos(\omega t) \quad (1)$$

134 where Q is the pumping rate (m^3/s), Q_{mean} is the pumping constant mean signal (m^3/s), Q_{amp} is
 135 the pumping constant amplitude of oscillation (m^3/s) and ω is the angular frequency (rad/s) also
 136 equal to $\frac{2\pi}{P}$ where P is the period (s).

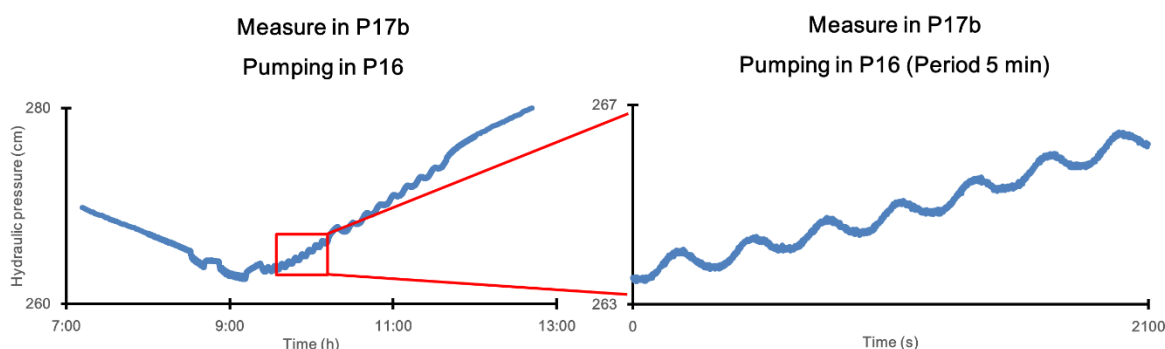
137 The harmonic pumping tests were led with $Q_{\text{mean}} = 8.8 \text{ L/s}$ and $Q_{\text{amp}} = 3.7 \text{ L/s}$ in P13, and with
 138 $Q_{\text{mean}} = 9.7 \text{ L/s}$ and $Q_{\text{amp}} = 4 \text{ L/s}$ in P16.

139 During these two pumping tests, the hydraulic level variations in 13 boreholes (including the
 140 two pumping boreholes) were continuously measured, in terms of pressure, with CTD Diver
 141 probes with an accuracy of $\pm 0.05 \text{ \%FS}$ (%FullScale).

142 2.3. Data processing

143 Figure 2 presents an example of hydraulic pressure measured in one well during the pumping
 144 test in P16. Data processing on the hydraulic level measurements needs to be realized in order
 145 to extract the specific oscillatory responses, in the different wells, to the oscillation induced by
 146 the pumping. These specific responses will be described in terms of amplitude and phase offset
 147 (relative to the pumping signal).

148



149

150 Figure 2: Graphs of the responses measured in P17b (during a pumping in P16) superposed on
 151 the tidal signal induced by the nearby Seine River. The left graph represents the responses
 152 measured during the entire pumping test in P16, while the right graph represents a zoom on the
 153 responses to the period of oscillation 5 min.

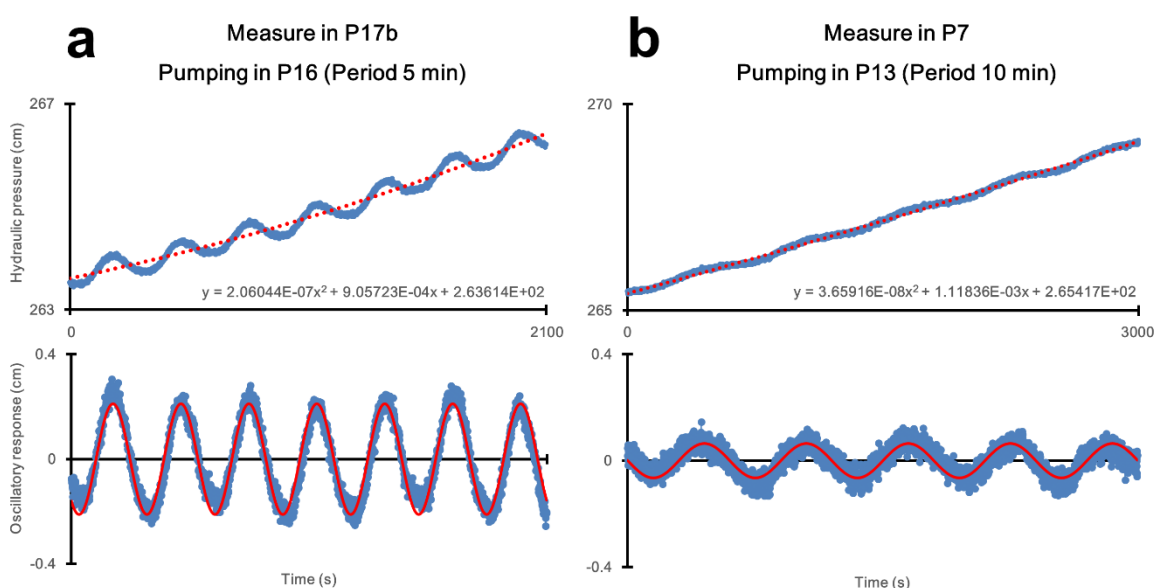
154

155 First, the global trend, mainly controlled by the Seine tidal signal is removed from the raw
 156 measurements, as presented in the two examples in Figure 3. At the time scale of the pumping

157 tests (max. 1 hour) the global trend can be assimilated to a second-order polynomial, adjusted
 158 to the measured data, which is then subtracted from the raw measurements. After this operation,
 159 only the noisy oscillatory responses to the oscillations of the pumping tests remain.

160 The second process consists of a Fast Fourier Transform (FFT) on the oscillatory responses in
 161 order to denoise the signal and interpret each oscillatory response in terms of amplitude and
 162 phase offset values, which are timeless and can be used in the oncoming frequency domain
 163 modeling. The FFT is performed in MATLAB with the FFT function which returns complex
 164 numbers used to calculate the amplitude and phase for each frequency of oscillation contained
 165 in the signal. It was then verified that, for each FFT performed, the interpreted oscillation was
 166 coherent with the measurement.

167



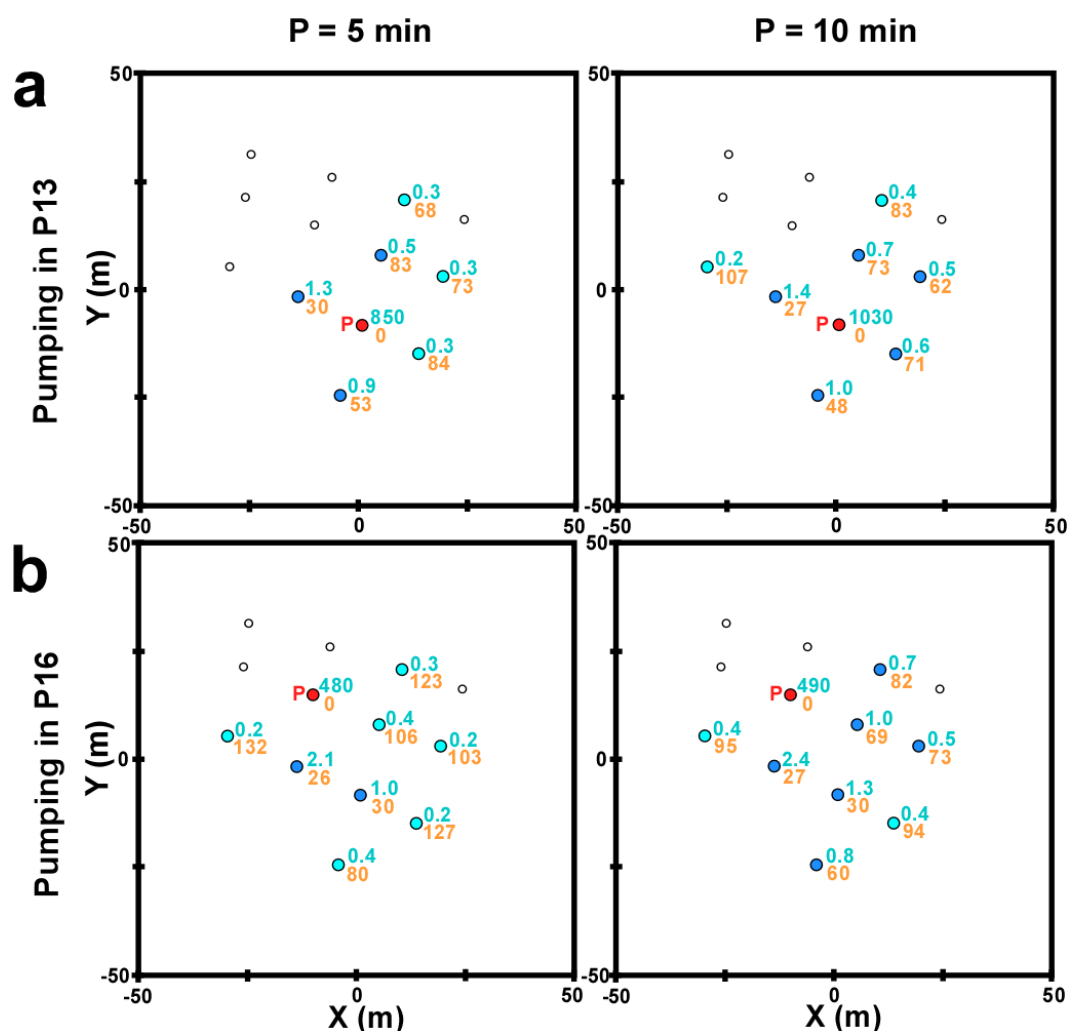
168

169 Figure 3: Graphs of the responses measured in **a** P17b (during a pumping in P16) and **b** P7
 170 (during a pumping in P13) as examples of the data processing performed on each measured
 171 response. The global trend is subtracted from the hydraulic pressure (this trend is approached
 172 with a quadratic equation as shown with the dotted red lines) to isolate the oscillatory response
 173 in each measurement. Then a FFT is performed on these oscillatory responses to interpret their
 174 amplitudes and phase offsets as purely sinusoidal signals (red lines).

175

176 Once the data processing has been performed for each measured well, a map of amplitude and
 177 phase offset responses can be produced (Figure 4). The amplitude and phase responses appear
 178 to be correlated: globally, a low amplitude response is associated to a high phase offset.
 179 Therefore, the amplitude of the signal is decaying when propagating away from the pumping
 180 well, while its phase offset increases. These amplitude and phase responses are related to the
 181 heterogeneity of the hydraulic properties of the aquifer. Thus, their distribution allows one to
 182 describe, qualitatively or quantitatively, the heterogeneity of the field site.

183



184

185 Figure 4: Maps of the amplitudes (in blue, in mm) and phase offsets (in orange, in $^{\circ}$) interpreted
 186 for each measurement point: **a** pumping in P13, **b** pumping in P16. The maps are presented for
 187 the two pumping wells (designated as a red 'P') and for the two periods of pumping signal (P
 188 = 5, 10 min.). Uncaptioned boreholes represent an absence of oscillatory response in the
 189 measurement (amplitude < 0.1 mm).

190

191 These maps permit visualization of the spatial evolution of the oscillatory responses for each
192 pumping well when the period of solicitation signal is modified. The heterogeneity of the study
193 site can already be perceived here, as the influence of each pumping does not propagate
194 circularly. In fact, the areas impacted by the pumping tests show particular directions of
195 propagations of the oscillatory signal. For example, for a pumping in P16 for the period 5 min,
196 the signal propagates mainly to the south and only with lower responses to the boreholes to the
197 east. This may highlight a preferential path of propagation southward from P16. However, for
198 the period 10 min, the responses remain localized to the south and east of the pumping location
199 but show more homogeneous responses in these two directions.

200 These oscillatory responses can be associated to an inversion process in order to quantitatively
201 characterize the heterogeneity and to estimate the spatial distribution of the properties over the
202 study site. It is then possible to check if the modeled property distributions can be correlated to
203 the known geology of the field site and the measured pollution appearance (frequency of
204 occurrence of floating NAPL), in order to better understand the propagation of the pollutants
205 throughout the site.

206 **3. Modeling strategy**

207 **3.1. Forward problem and model parameterization**

208 For the modeling part, the aquifer and the flows are considered to be two-dimensional (2D; top-
209 down view). In fact, geologically, the main spatial variation is generated by the existence of
210 localized deposits of flint and chalk blocks, which are always intersected at the same depths (6
211 m to 9 m) by some boreholes. Furthermore the groundwater flows generated by the pumping
212 tests induced generally horizontal streams. In fact, the most important drawdowns (30 cm to 1
213 m), which are associated to vertical flows, were localized only at the pumping wells, whereas,

214 over the rest of the field site, the drawdowns were of an order to magnitude of millimeters (see
 215 Figure 4).

216 The 2D forward problem, hereafter noted f , in the frequency domain, permits one to simulate
 217 the spatial amplitude and phase offset responses to a pumping signal from property values
 218 distributed over the plan model and from the following equation of flow continuity (associated
 219 to Darcy's law) (Cardiff et al. 2013):

$$220 \quad i \omega S_s H_\omega - \nabla \cdot (K \cdot \nabla H_\omega) = \frac{Q_{\text{amp}}}{V_{\text{el}}} \delta(x - x_q, y - y_q) \quad (2)$$

221 where S_s is the specific storage (1/m), K is the conductivity (m/s), H_ω is a complex parameter
 222 holding the spatial amplitude and phase offset responses in the frequency domain, i is the
 223 imaginary unit, Q_{amp} is the amplitude of oscillation in the rate of a harmonic pumping (m^3/s)
 224 led at a coordinate (x_q, y_q) , δ is the Dirac distribution and V_{el} is an elementary volume from
 225 the finite element mesh of the model associated to the pumping locations.

226 One considers $H_\omega(x, y) = 0$ at the boundaries of the model as the boundary condition and all
 227 over the model as the initial condition. In order to reduce the effect of the boundary conditions
 228 on the simulations in the field area, it was necessary to enclose the area of interest in the model
 229 in a larger buffer zone ($500 \times 500 \text{ m}^2$) associated with uniform regional hydraulic properties,
 230 thus moving the boundaries away from the areas impacted by the pumping tests in the models.
 231 In this work, Equation (2) was solved on a triangular finite element mesh with COMSOL
 232 Multiphysics. The meshing is adaptive, which means that it is refined automatically around the
 233 borehole locations in the model. The mesh in the model is composed of 26,616 triangular
 234 elements.

235 The amplitude and phase offset responses over the model can then be extracted from the
 236 complex parameter H_ω as follows:

$$237 \quad A(x, y) = \sqrt{(\operatorname{Re}H_\omega(x, y))^2 + (\operatorname{Im}H_\omega(x, y))^2} \quad (3)$$

238 with A the amplitude response (m), and Re and Im the functions returning respectively the real
 239 part and the imaginary part of H_ω .

$$240 \quad \Phi(x, y) = \frac{180}{\pi} \operatorname{atan2}(-\operatorname{Im}H_\omega(x, y), \operatorname{Re}H_\omega(x, y)) \quad (4)$$

241 with Φ the phase offset response ($^\circ$) and $\operatorname{atan2}$ the inverse tangent function with two arguments
 242 (rad).

243 Here, the frequency domain permits performance of a timeless simulation of the oscillation
 244 signals and saves a consequent amount of time compared to modeling in the time domain,
 245 especially for the inversion.

246 **3.2. Inverse problem**

247 The inverse problem involves a forward problem in order to link the distribution of the property
 248 values in the model (contained in a m -vector \mathbf{p}) to the simulated amplitude and phase
 249 responses (contained in a n -vector \mathbf{d}): $\mathbf{d} = f(\mathbf{p})$. The forward problem is then seen as an
 250 application $f: \mathbb{R}^m \rightarrow \mathbb{R}^n$. The aim of the inverse problem is to find a distribution of property
 251 values which minimizes the difference between the measured and the simulated responses. This
 252 goal can be achieved by minimizing the following objective function:

$$253 \quad \Psi = \frac{1}{2} (\mathbf{d}_{\text{obs}} - \mathbf{d})^T \cdot \mathbf{C}_d^{-1} \cdot (\mathbf{d}_{\text{obs}} - \mathbf{d}) + \frac{1}{2} (\mathbf{p}_{\text{prior}} - \mathbf{p})^T \cdot \mathbf{C}_p^{-1} \cdot (\mathbf{p}_{\text{prior}} - \mathbf{p}) \quad (5)$$

254 where \mathbf{p} and $\mathbf{p}_{\text{prior}}$ are m -vector containing respectively the distribution of the property values
 255 (here transmissivity and storativity) over the model and their a priori values, \mathbf{d}_{obs} is a n -vector
 256 containing the measured responses and \mathbf{d} is a n -vector containing the responses simulated
 257 from the forward problem (here amplitudes and phases). \mathbf{C}_d is a $(n \times n)$ covariance matrix on
 258 the data, including the uncertainties on the observed and simulated data, and \mathbf{C}_p is a $(m \times m)$
 259 covariance matrix on the property values.

260 In a deterministic inverse problem, the minimization of Equation (5) is performed iteratively,
 261 starting from an acceptable assumption of property values in \mathbf{p} . Then, for each iteration of the
 262 inversion, a sensitivity analysis of the distributed property values to the simulated data is
 263 operated by computing the Jacobian of the operator f :

$$264 \quad \mathbf{J}_k(i, j) = \left. \frac{\partial f_i}{\partial \mathbf{p}_k} \right|_{\mathbf{p}_k(j) = \mathbf{p}_k(j) + \Delta p} \quad (6)$$

265 with \mathbf{J}_k the $(n \times m)$ Jacobian matrix computed at an iteration k using a finite difference method
 266 and Δp is the finite difference step. It can be noted that the same sensitivity analysis can be
 267 also performed with an adjoint state approach, as described in Cardiff et al. (2013), which is
 268 generally less demanding in computation time.

269 The property values are then optimized, at an iteration k , from a linearization of the objective
 270 function:

$$271 \quad \mathbf{p}_{k+1} = \mathbf{p}_k + \left((\mathbf{J}_k)^T \cdot \mathbf{C}_d^{-1} \cdot \mathbf{J}_k + \mathbf{C}_p^{-1} \right)^{-1} \times \left((\mathbf{J}_k)^T \cdot \mathbf{C}_d^{-1} \cdot (\mathbf{d}_{\text{obs}} - \mathbf{d}) + \mathbf{C}_p^{-1} \cdot (\mathbf{p}_{\text{prior}} - \mathbf{p}_k) \right) \quad (7)$$

272 At the end of each iteration the value of the objective function is recalculated and the iterative
 273 process continues until the inversion has reached a sufficient minimization of the objective
 274 function.

275 After the last iteration, the posterior variances on the different optimized values of properties
 276 can be estimated by computing the posterior covariance matrix:

$$277 \quad \mathbf{C}_{p,\text{post}} = \left(\left(\mathbf{J}_{\text{post}} \right)^T \cdot \mathbf{C}_d^{-1} \cdot \mathbf{J}_{\text{post}} + \mathbf{C}_p^{-1} \right)^{-1} \quad (8)$$

278 where $\mathbf{C}_{p,\text{post}}$ is the $(m \times m)$ posterior covariance matrix and \mathbf{J}_{post} is the covariance matrix
 279 computed during the last iteration. The diagonal entries of this matrix hold the posterior
 280 variances associated to each property value in the model, thus allowing for the establishment
 281 of uncertainty maps on the inverted property values.

282 **3.3. Inversion parameters**

283 Two separate inversions have been led with the responses associated to the two different periods
 284 of pumping signals ($P = 5$ and 10 minutes). This means that, for each separate inversion, both
 285 pumping test (P13 and P16) responses to one period of signal (5 or 10 min) are considered.
 286 Therefore, each separate inversion is led with a dataset of 26 couples of amplitude / phase-offset
 287 measured responses. Afterwards, a joint inversion, integrating the responses to the two periods
 288 of signals simultaneously, also for both pumping tests (P13 and P16), has been performed (with
 289 a dataset of 52 couples of amplitude / phase-offset measured responses).

290 The aim of these inversions was to image the 2D hydraulic properties of the study area ($100 \times$
 291 100 m^2). Therefore 2D models of transmissivity (T) and storativity (S) were built, wherein
 292 the property values are distributed over a grid of m squared cells. In the inversion process, the
 293 property values were integrated in the form of \log_{10} values in \mathbf{p} and $\mathbf{p}_{\text{prior}}$, which allows for
 294 more stability.

295 The inversions were initialized with uniform models of properties ($T = 10^{-3} \text{ m}^2/\text{s}$ and $S = 10^{-3}$).
 296 The same property values were also kept as prior information in the inversion process and for
 297 the regional buffer zone. These means that property values were chosen accordingly to a global

298 site knowledge from pumping investigations at higher scale. Therefore, they represent a
 299 reasonable global estimate to begin the inversion and for the large-scale flows in the buffer
 300 zone.

301 For these inversions, \mathbf{C}_p and \mathbf{C}_d were considered as diagonal matrices, with $\mathbf{C}_p = 0.1 \times \text{Id}(m)$
 302 and $\mathbf{C}_d = \sigma^2 \times \text{Id}(n)$ where $\sigma = 0.1$ mm for the amplitude responses and $\sigma = 5^\circ$ for the phase
 303 offset responses, and Id represents the identity matrix. It was decided not to integrate a
 304 variogram constraint on the distribution of the properties in the inversion, as it was foreseen
 305 that this distribution could be locally contrasted, which is incompatible with the smoothness
 306 brought by such constraint. In fact a variogram constraint would force a smooth distribution of
 307 the property values. However, the S values were constrained to remain within a range of
 308 $10^{-1} < S < 10^{-5}$ in order to avoid unphysical values that could occur due to the absence of such
 309 geostatistical constraints in the inversion. $\Delta p = 10^{-5}$ was taken for the Jacobian computation.

310 **4. Results**

311 **4.1. Property maps**

312 The results of the different inversions are presented in term of maps of distributed transmissivity
 313 and storativity values in Figure 5, in term of maps of diffusivity (calculated from the maps of
 314 transmissivity and storativity: $D = \frac{T}{S}$) values in Figure 6, and in term of root mean square error
 315 (RMSE) between the measured and simulated amplitudes and phase-offsets in Table 1. Figure
 316 7 also presents the maps of uncertainties on the inverted property values and the scatterplots
 317 obtained on the datasets after the inversions.

318 Each separately inverted model allows for a good reproduction of the amplitude responses (0.1
 319 to 0.3 mm RMSE) and the phase-offset responses (1° to 3° RMSE). The reproduction of the
 320 responses with amplitudes less than 1 mm appear to be less accurate (Figure 7). However, as

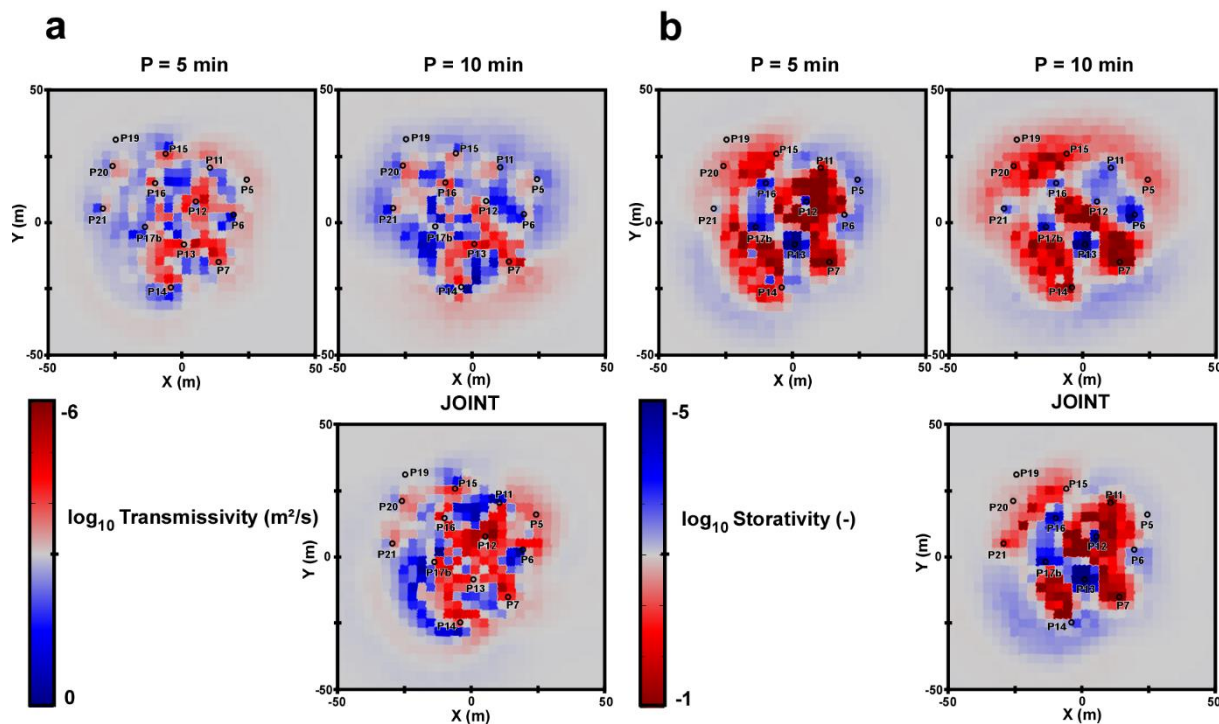
321 these responses approach the probe's measurement limits, they may be noisy and less relevant
 322 for an exact reproduction in the inversion. The result of the joint inversion presents a slight
 323 increase in the RMSE between the responses simulated with the model and the measurements,
 324 mostly on the amplitudes. It appears that this increase is mainly due to the responses from one
 325 borehole (P11 when pumping in P16) for which the amplitudes cannot be well reproduced for
 326 the two periods simultaneously. If one does not consider this borehole, the amplitude RMSE
 327 from the joint inversion becomes 0.3 mm. However the phases from these two boreholes remain
 328 well reproduced with the distribution in the joint inversion. Furthermore, an attempt was made
 329 at improving the amplitude reproduction in the joint inversion, which then resulted in a very
 330 bad misfit for the phase responses. Therefore, reproduction of the responses presents a globally
 331 satisfying compromise between amplitudes and phases, especially regarding the complexity of
 332 the study area.

333

334 Table 1: Results of the separate and joint inversions: size of the property cells in the grid and
 335 RMSEs on the amplitude (Amp. RMSE) and phase-offset (P.-O. RMSE) responses.

Inversion	Cell size	Amp. RMSE	P.-O. RMSE
$P = 5$ min	3.3×3.3 m ²	0.2 mm	1 °
$P = 10$ min	3.3×3.3 m ²	0.3 mm	3 °
Joint	3.3×3.3 m ²	0.6 mm	4 °

336



337

338 Figure 5: Maps of the distribution of **a** transmissivity and **b** storativity obtained with the
 339 separate inversions per period ($P = 5, 10$ min.) of pumping signals and the joint inversion.

340

341 The property maps remain globally similar between the separate inversions and the joint
 342 inversion, showing a certain coherence of the datasets generated with different periods of
 343 oscillation. The T and S maps show very high heterogeneities within the field site, with
 344 important local variations and large ranges of values. This contrasted property distribution and
 345 the large range of values can be linked to the known geology and especially the observed high
 346 velocity flows that can exist within the coarse sands and flint blocks unit. Local transmissivity
 347 estimates from the joint inversion result were compared to measurements made at four locations
 348 (P6, P11, P14 and B4, a borehole located midway between P16 and P17b) by De Clercq et al.
 349 (2020) and are shown in Table 2. These estimates were made by integrating the inverted values
 350 in circles of 1-m diameter centered on the different locations. The inverted transmissivities are
 351 close to the measured ones. Except for P11, the transmissivity estimates appear as slightly
 352 underestimated.

353 The transmissivity fields present higher values on the west side of the area, lower values on the
 354 east side, and also decrease at the borehole locations, possibly indicating borehole effects on
 355 the flows. A similar degree of heterogeneity has been observed in the 3D conductivity field
 356 inverted from constant-rate pumping tests conducted on this site by De Clercq et al. (2020). In
 357 this 3D map, the heterogeneity is located mostly at the depths of the flint block unit, also
 358 suggesting that this unit may be responsible for the complex flows occurring on this site.
 359 Comparing these maps of transmissivity distribution to the conductivity model, they appear to
 360 be globally coherent, especially considering this study's result for a 10-min period, showing a
 361 more conductive path along P6 and P12. The conductivity model also suggests a continuous
 362 low-conductivity path from P14 to P21, to P20 and to P19, and a more conductive area than in
 363 this study's results around P7.

364 The highest values of storativity are grouped in three zones around P7, P14 and P15/P20/P19.
 365 In contrast, the lowest values of storativity seem to delineate a connectivity between P13, P17b,
 366 P16 and P15 for $P=5$ min (and P21 and P6 for $P=10$ min). These six boreholes are all located
 367 in the flint blocks unit (Figure 1), which might be continuous between them, and thus inducing
 368 a preferential flow connection. However, P20 is not associated with this connectivity in the
 369 model, whereas this borehole intersects the unit. This might be due to the fact that, if high flows
 370 can occur in this unit, they are not necessarily connected. The results obtained with the joint
 371 inversion indicate a less direct connectivity than suggested in $P=10$ min between P16 and P6,
 372 but a higher connectivity in the direction of P21 than suggested in $P=5$ min.

373

374 Table 2: Comparison between transmissivities measured at several locations (De Clercq et al.
 375 2020) and transmissivities assessed from the joint inverted distribution.

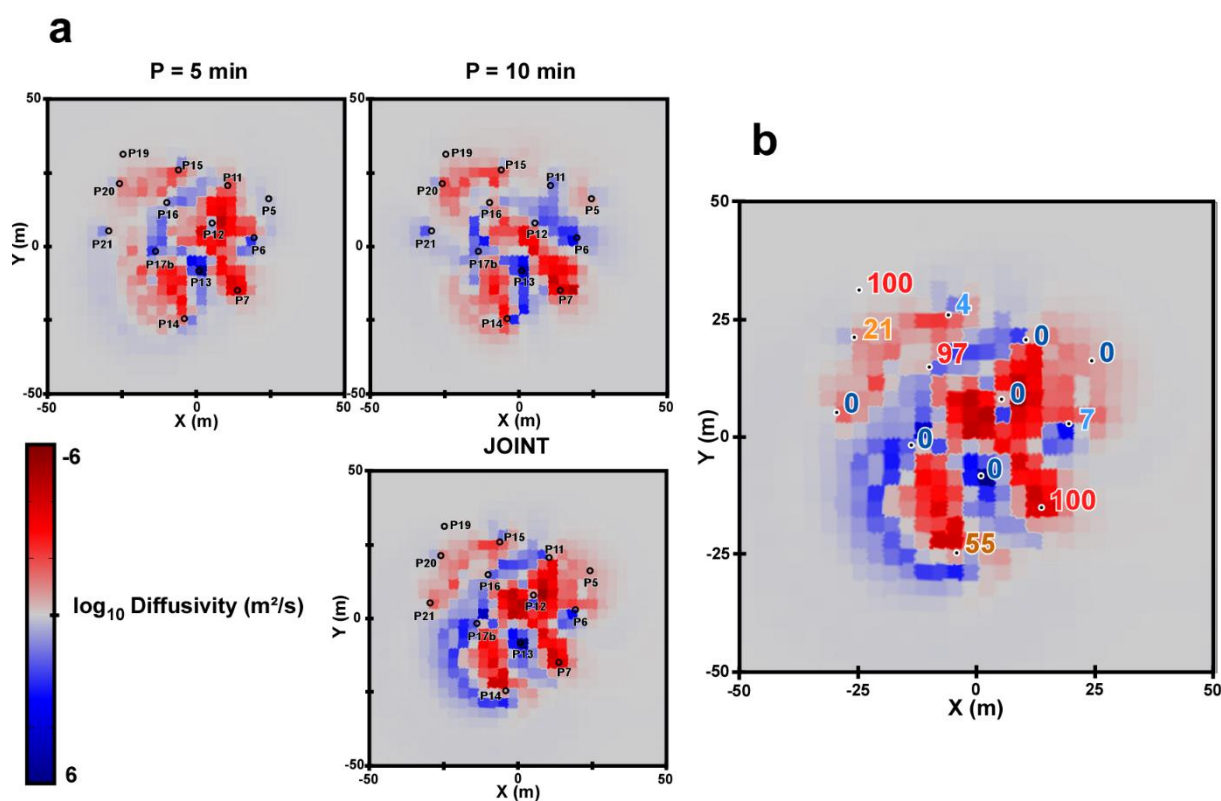
Location	$\log_{10}(T)$ measured	$\log_{10}(T)$ inverted	Variation
P14	-3.70	-3.85	-0.15
P11	-3.01	-2.60	+0.41

P6	-2.93	-3.16	-0.23
B4 (between P16 and P17b)	-2.41	-2.76	-0.35

376

377 The coherence of the property distributions in the models can also be discussed by comparing
 378 the inverted maps of diffusivity (Figure 6) to the frequencies of occurrence of observed floating
 379 NAPL in each borehole of the field site.

380



381

382 Figure 6: **a** Maps of the distribution of diffusivity (T/S) obtained with the separate inversions
 383 per period ($P = 5, 10$ min.) of pumping signals and the joint inversion. **b** Map presenting, for
 384 each borehole, the value of frequency of occurrence of observed floating NAPL (in %),
 385 superposed on the diffusivity map obtained with the joint inversion.

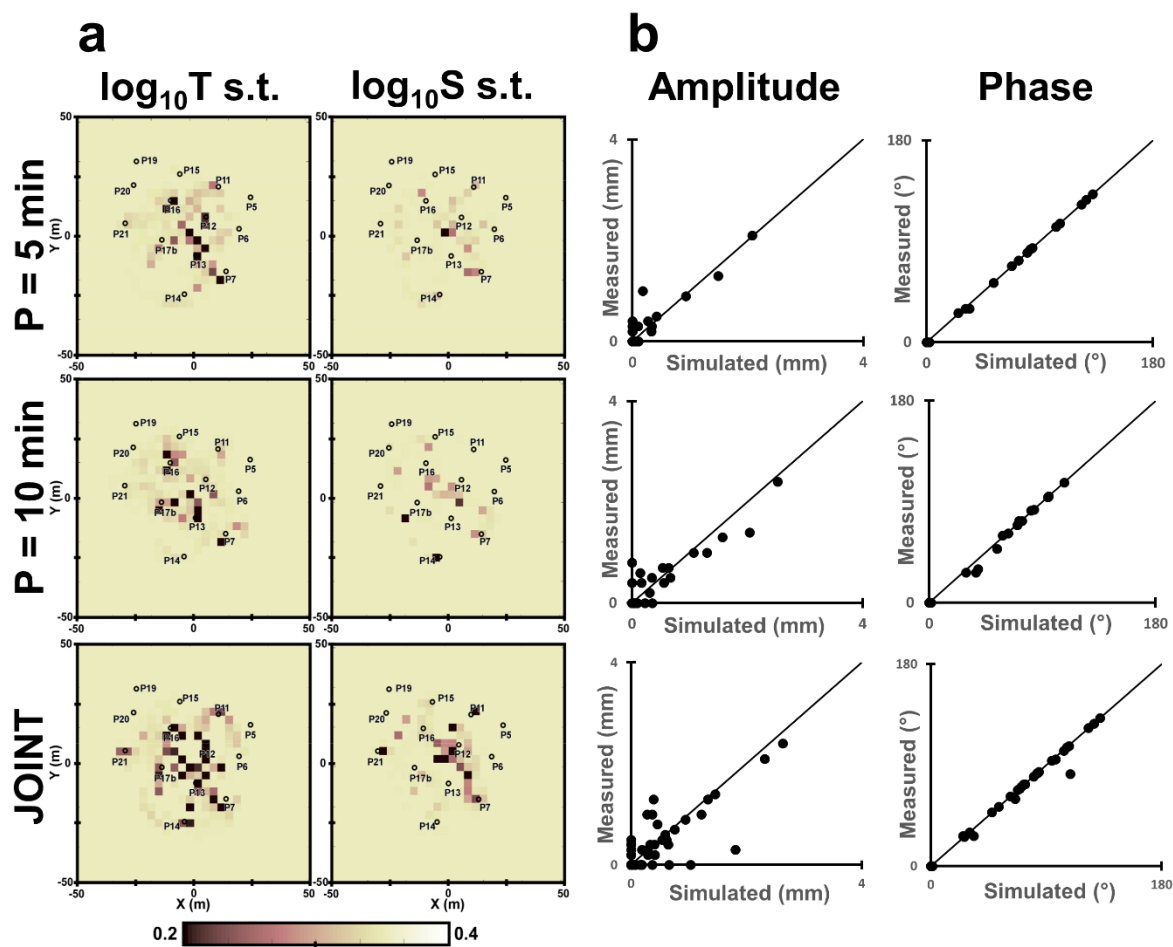
386

387 The diffusivity maps (Figure 6) generated by the inversions with periods of oscillation of 5 and
 388 10 min image a globally similar heterogeneity over the field site. A path of more important
 389 diffusivity appears along P13, P17b and P16. The responses to the period of signal 10 min

390 provide different information tending to indicate that this path continues beyond P16 and P17b,
391 to P6 and P21. As for the S maps, this path seems to be geologically coherent as, in their logs,
392 P13, P17b, P16, P21 and P6 intersect the unit of coarse sands and flint blocks.

393 The diffusivity map obtained with the joint inversion tends to reduce the importance of the
394 diffusivity path toward P6 suggested in the result $P=10$ min, while confirming the path toward
395 P21 appearing on the same result. The diffusivity map can be linked to the values of frequency
396 of occurrence of observed floating NAPL in each well (Figure 6). In fact, the wells in which
397 floating NAPL is frequently observed are almost systematically associated to areas of low
398 diffusivity in the model, except P15. In contrast, almost all wells in which no NAPL is observed
399 are located on the continuous diffusive path imaged by the model, except P5. As the water table
400 in this field site is constantly moving with the tide signal, it is believed that floating NAPL may
401 be more likely entrapped in low-diffusivity areas.

402



403

404 **Figure 7: a** Uncertainty maps (standard deviations on the T and S exponents) and **b** scatterplots
 405 of simulated vs. measured amplitudes and phases obtained for each separate inversion and the
 406 joint inversion.

407

408 The uncertainty maps in Figure 7 indicate that the joint inversion is better constrained than the
 409 two separate ones, showing that the responses to the two different periods of oscillation carry
 410 different information, as suggested in Cardiff et al. (2013). It is interesting to observe that the
 411 less uncertain areas in the T fields are located along the path of highest diffusivity in Figure 6,
 412 while the less uncertain areas in the S fields are more likely located in the zones of lowest
 413 diffusivity.

414 It was not possible to directly validate the values of T and S obtained in the inverted maps
 415 with field data. However, their similar distribution in the results of the separate and the joint

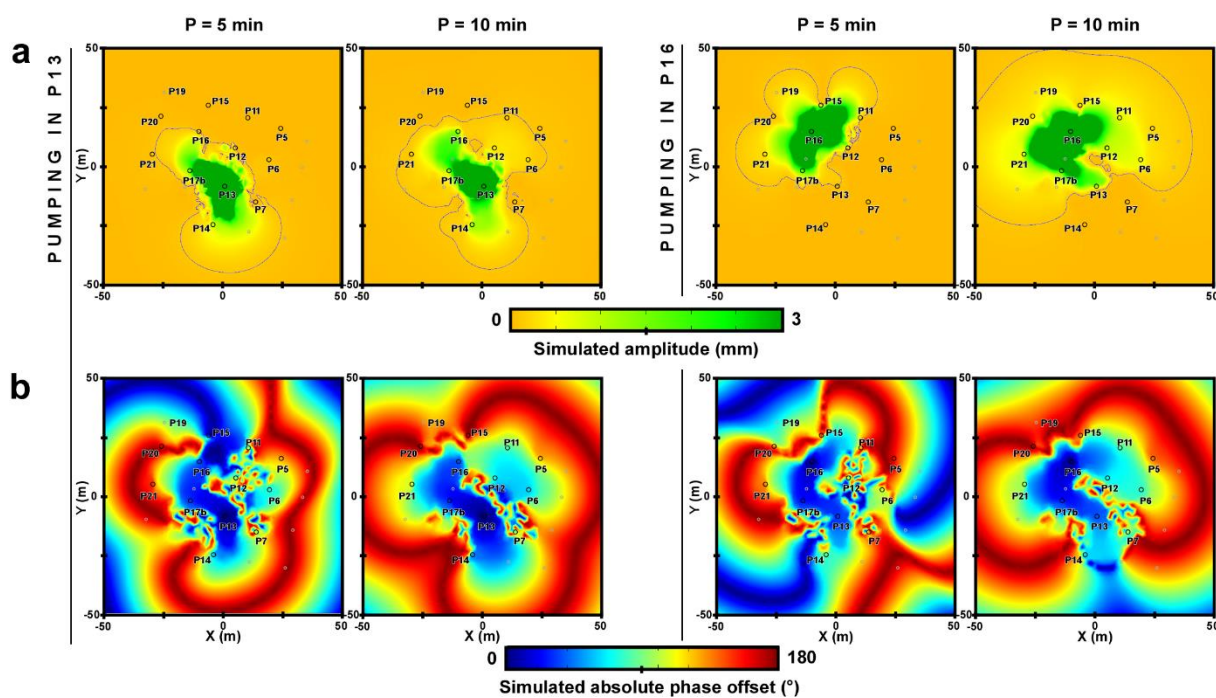
416 inversions appeared as coherent regarding the given knowledge on the geology of the field site
417 and its behavior to contaminant mobility.

418 **4.2. Simulations**

419 This section discusses the maps of the amplitude and phase-offset spatial responses (Figure 8)
420 simulated with the property maps obtained from the separate inversions and presented in the
421 previous section (Figure 5). These maps present the propagation of the oscillatory signal in the
422 field. The amplitude of the oscillation is presented with a green color showing the highest
423 amplitude responses (near to the pumping point) and an orange color in the area of the site
424 where the signal has lowered ($< 1\text{mm}$) or totally attenuated. The phase of the oscillation is
425 indicated with a low offset (in blue), near the pumping point, and with high offsets (in red).
426 Notice that the offset is cyclic, meaning that the signal response can be in phase with the
427 pumping point even at a long distance from it, but with one (or more) oscillation cycle delay.
428 However this is purely theoretical, as at such distances the signal has generally a too low
429 amplitude to be measured.

430 A clear evolution is visible in the interpreted simulations of the responses to an increasing
431 period of signal. The impacted area tends to increase with the period of oscillation, although
432 the amplitude of pumped flow rate remains the same. In fact, for a period of oscillation of 10
433 min, low amplitude responses appear in areas around the pumping locations that were not
434 impacted with a period of oscillation of 5 min.

435



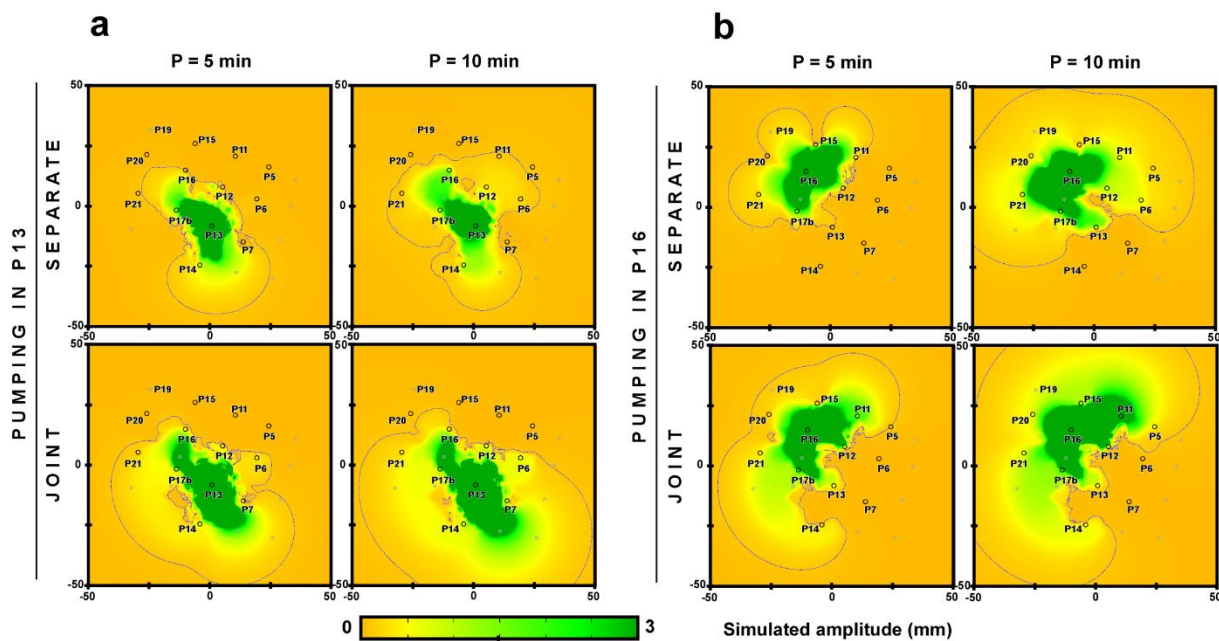
436

437 **Figure 8:** Maps of **a** amplitude and **b** phase offset responses simulated over the study site with
 438 the inverted property distributions. These maps are presented for the two pumping wells and
 439 for the two periods of pumping signal ($P = 5, 10$ min.). The grey isolines in the amplitude maps
 440 represent the limit to amplitudes < 0.1 mm.

441

442 A comparison between the simulations of the measured responses obtained for each separate
 443 inversion and the joint inversion is presented in Figure 9. The comparison focuses on the
 444 amplitude responses, which are easier to visualize than the phase-offset responses.

445



446

447 Figure 9: Comparison of the maps of amplitude responses simulated over the study site with
 448 the property distributions from the separate inversions ($P = 5, 10$ min.) and from the joint
 449 inversion. These maps are presented for the two pumping wells (**a** P13, **b** P16) and for the two
 450 periods of pumping signal ($P = 5, 10$ min.). The grey isolines in the amplitude maps represent
 451 the limit to amplitudes < 0.1 mm.

452

453 In the simulations made with the result of the joint inversion, when increasing the period of
 454 oscillation, an increase of the area impacted by the generated oscillatory signal is visible; this
 455 was observed previously in the simulations made with the results of the separate inversions.

456 By comparing the simulations made from the joint and separate models, it appears that, in the
 457 joint simulations, the areas associated to the higher amplitudes are close to the ones obtained in
 458 the $P=5$ min separate simulations. However the areas associated to low amplitude responses are
 459 more extended in the joint simulations, closer to the simulations obtained with the $P=10$ min
 460 models. These observations would tend to indicate that the lower period would rather mobilize
 461 flows associated to close conductive areas, while higher periods would mobilize flows in more
 462 extended areas, generating more low amplitude responses.

463 5. Discussion

464 The use of oscillatory data to characterize the spatial hydraulic properties of the study site
465 permitted successful creation of an image of the high heterogeneity existing at this scale in the
466 aquifer. Furthermore, using oscillatory data here provided three main advantages. Firstly,
467 oscillatory data present advantages compared to pumping responses analyzed in a temporal
468 domain, as the oscillatory responses can be simulated in a model in the frequency domain,
469 leading to quick computation time, equivalent to simulations in a steady state, while also
470 characterizing both T and S . Furthermore, compared to pumping tests aiming to reach a steady
471 state, the global pumping duration can generally be reduced as, in this case, 6-7 generated
472 oscillations are sufficient to extract exploitable responses. Secondly, the oscillatory responses
473 could be easily extracted from the field natural signal which is highly influenced by the tidal
474 signal of the nearby river (through a FFT). This was less the case for drawdown curves of
475 constant pumping rates led on the same site, for which the extraction of the responses became
476 problematic (in particular, separating the tide signal is not as easy as extracting pure oscillation
477 signals without long-term measurements). Thirdly, oscillatory pressure signals propagate in
478 water, and their spatial responses are extractable, even with low amplitudes (mm amplitudes at
479 a field scale in this study). This property was useful in this study case as, due to the high
480 heterogeneity of the field site, some pumping wells on the site show a quick growth of their
481 drawdown when increasing the pumping rate, which can sometimes lead to an emptying of the
482 well. Thus, in such pumping wells, oscillatory pumping allowed for a spatial characterization
483 with low pumping rates (also beneficial in this case as the study site is contaminated).
484 Moreover, with oscillatory signals, various distances impacted by the pumping can be explored
485 without having to increase the pumping rate. In fact, as shown in these results, the area impacted
486 by the pumping can be extended by increasing the period of the oscillatory signal.

487 Similar behavior was observed by Cardiff et al. (2013) in their tomography on a synthetic
488 heterogeneous case at a decametric scale, with periods of oscillations of 5 s to 5 min. They
489 concluded that higher frequencies could provide better information on the properties around the
490 wells, while lower frequencies provided more information on areas beyond the well locations.
491 Therefore they suggested performing joint inversions to combine the information carried by
492 both higher and lower frequencies. When applying oscillatory signals in a karstic aquifer,
493 Fischer et al (2018) noticed that with lower periods of oscillatory signals, the responses seemed
494 to hold more specific information about the most conductive paths in the aquifer (karstic
495 conduits), while with higher periods the responses were affected also by flows in less
496 conductive paths (fractures and fissures in the rock). Similar behavior was already suggested
497 by Rabinovich et al. (2015), who used a simple model to show that higher frequencies would
498 generate flows more specifically in the most conductive areas of an aquifer. This could also
499 explain why the conductivity distributed model interpreted from constant-rate pumping tests
500 led on the same site as that used by De Clercq et al. (2020) is closer to this study's transmissivity
501 map inverted with the highest period (10 min) measurements (a constant signal being
502 comparable to a signal with an infinitely high period).

503 The results of hydraulic imaging from this study, obtained from responses to oscillatory signals
504 at different periods, tend to validate these observations. When performing a joint inversion, as
505 described by Cardiff et al. (2013), the result appears better constrained, suggesting that the
506 information from the different periods is non redundant. In this application in an alluvial
507 aquifer, the main difference in the information held by the responses to different periods of
508 oscillations appears to be the area of groundwater impacted by the oscillatory signal. Therefore,
509 with lower periods, the oscillatory signal impacted mostly conductive zones near the pumping
510 wells, and with higher periods, the signal also generated low responses around the pumping
511 wells, in less conductive areas. In a recent application comparing the results obtained on the

512 same site with oscillatory data and constant-rate data, Cardiff et al. (2019) observed that the
513 characterization with oscillatory data provided lower conductivity values in the zone associated
514 to low conductivities, thus accentuating the contrast between high and low conductivity
515 distribution. This could be explained by the fact that low-period oscillations generate responses
516 with spatial distributions highly dependent on the contrast existing in the property distribution
517 around the pumping well.

518 In this application, the oscillatory responses were extracted from a background tide signal. An
519 eventual impact of the tide signal on the groundwater condition (groundwater level) during the
520 pumping has been considered as negligible. This is mainly due to the fact that the background
521 tide signal, throughout the pumping tests, generated a movement of the water table not
522 exceeding 10 cm ($< 2\%$ of the water column). Nevertheless, it is known that during the most
523 influential sea tide ranges at this field site, the groundwater level can naturally move up to 1 m,
524 which then might have an impact on the groundwater condition. Therefore, before performing
525 a pumping investigation, it has been important to firstly study the movements induced by the
526 natural tide signal on the groundwater level of this field site, without any other solicitation. It
527 can also be noticed that the sea tidal signal (comparable to an oscillation) itself could be
528 considered as a signal for the field characterization, thus also totally avoiding the need to pump
529 in the aquifer. However, its important period (about 12 h) would be rather more interesting for
530 characterization of sites of larger areas, for example a site at a kilometric scale, as presented in
531 Jardani et al. (2012). It was also hypothesized that the main flows were horizontal in this alluvial
532 aquifer and Darcy's law was employed to simulate these flows. The authors believe that this
533 assumption is correct for a major part of the field site. However, locally at the pumping
534 boreholes, some vertical flows might occur. In particular, a participation of the underlying chalk
535 aquifer is possible at the pumping locations, explaining why the amplitude responses are more
536 distinct at the pumping locations than at the other wells of the field site.

537 **6. Summary and conclusion**

538 Natural or induced oscillatory signals in hydraulic tomography have been a topic of interest for
539 field characterization in hydrogeology for several years. Theoretical developments and field
540 applications have shown the advantages brought by these signals.

541 The results of the characterization described here, led with responses to oscillatory pumping
542 signals in a complex alluvial aquifer, allowed for an imaging of the heterogeneity of the
543 subsurface properties at the decametric scale. Responses to two different periods of oscillations
544 (5 and 10 min) were used. The results show that increasing the period of oscillation results in
545 an increase of the area impacted by the oscillatory signal induced by the pumping test. The
546 lowest period of signals (5 min) provided more information on the conductive areas close to the
547 pumping wells, while the highest (10 min) permitted better characterization of the less-
548 conductive areas around the pumping location, with the low amplitude responses. Performing
549 a joint inversion with all data obtained with the two periods of oscillations results in less-
550 uncertain property maps than the ones obtained with separate inversions, thus confirming the
551 fact that both datasets carry different and complementary information.

552 Oscillatory signals provided, for this application, several advantages. Firstly, spatial responses
553 are exploitable only after several oscillations (6-7 in this case), thereby allowing for a reduction
554 in the pumping time. Then, the ability to solve the model in a frequency domain with the
555 oscillatory responses, rather than in a time domain, permits a considerable reduction in the
556 computation time required for the inversion. Secondly, the data processing allows extraction of
557 the responses even in an environment with a strong natural forcing, like in this case the tidal
558 variation induced by the nearby Seine River. Finally, the pumping rates can be globally lowered
559 as, for example in this case, an oscillation's amplitude of an order of magnitude of millimeter

560 can be extracted from measured responses with global decimetric variations through a FFT
561 process.

562 **Acknowledgments**

563 We would like to thank the Region Normandie and the Agence De l'Environnement et de la
564 Maîtrise de l'Energie (ADEME) for having financially supported this study.

565 **References**

566 Bakhos T., M. Cardiff, W. Barrash, P.K. Kitanidis. 2014. Data processing for oscillatory
567 pumping tests. *Journal of Hydrology* 511: 310-319.

568

569 Batu V. 1998. *Aquifer Hydraulics*. Wiley.

570

571 Berg S.J., W.A. Illman. 2015. Comparison of Hydraulic Tomography with Traditional Methods
572 at a Highly Heterogeneous Site. *Groundwater* 53: 71-89.

573

574 Bohling G.C., J.J. Butler Jr, X. Zhan, M.D. Knoll. 2007. A field assessment of the value of
575 steady state hydraulic tomography for characterization of aquifer heterogeneities. *Water*
576 *Resources Research* 43: W05430.

577

578 Butler J.J. 2005. Hydrogeological methods for estimation of spatial variations in hydraulic
579 conductivity. In: Y. Rubin, S.S. Hubbard. *Hydrogeophysics*. Water Science and Technology
580 Library. Springer, Dordrecht.

581

582 Cardiff M., W. Barrash, P.K. Kitanidis, B. Malama, A. Revil, S. Straface, E. Rizzo. 2009. A
583 Potential-Based Inversion of Unconfined Steady-State Hydraulic Tomography. *Ground Water*
584 47: 259-270.

585

586 Cardiff M., T. Bakhos, P.K. Kitanidis, W. Barrash. 2013. Aquifer heterogeneity
587 characterization with oscillatory pumping: Sensitivity analysis and imaging potential. *Water*
588 *Resources Research* 49: 5395-5410.

589

590 Cardiff, M., W. Barrash. 2015. Analytical and Semi-Analytical Tools for the Design of
591 Oscillatory Pumping Tests. *Groundwater* 53: 896-907.

592

593 Cardiff M., C. Slayer. 2016. Strategies for avoiding errors and ambiguities in the analysis of
594 oscillatory pumping tests. *Journal of Hydrology* 540: 1016-1021.

595

596 Cardiff, M., Y. Zhou, W. Barrash, P.K. Kitanidis. 2019. Aquifer Imaging with Oscillatory
597 Hydraulic Tomography: Application at the Field Scale. *Groundwater*. doi:
598 10.1111/gwat.12960.

599

600 De Clercq, T., A. Jardani, P. Fischer, L. Thanberger, T.M. Vu, D. Pitaval, J.-M. Côme, P.
601 Begassat. 2020. The use of electrical resistivity tomograms as a parameterization for the
602 hydraulic characterization of a contaminated aquifer. *Journal of Hydrology* 587: 124986.

603

604 D’Oria M., A. Zanini, F. Cupola. 2018. Oscillatory Pumping Test to Estimate Aquifer
605 Hydraulic Parameters in a Bayesian Geostatistical Framework. *Mathematical Geosciences* 50:
606 169-186.

607

608 Fischer P., A. Jardani, A. Soueid Ahmed, M. Abbas, X. Wang, H. Jourde, N. Lecoq. 2017.
609 Application of large-scale inversions algorithms to hydraulic tomography in an alluvial aquifer.
610 *Groundwater* 55: 208-218.

611

612 Fischer P., A. Jardani, H. Jourde, M. Cardiff, X. Wang, S. Chedeville, N. Lecoq. 2018.
613 Harmonic pumping tomography applied to image the hydraulic properties and interpret the
614 connectivity of a karstic and fractured aquifer (Lez aquifer, France). *Advances in Water*
615 *Resources* 119: 227-244.

616

617 Gultinan E., M.W. Becker. 2015. Measuring well hydraulic connectivity in fractured bedrock
618 using periodic slug tests. *Journal of Hydrology* 521: 100-107.

619

620 Hochstetler D.L., W. Barrash, C. Leven, M. Cardiff, F. Chidichimo, P.K. Kitanidis. 2016.
621 Hydraulic Tomography: Continuity and Discontinuity of High-K and Low-K Zones.
622 *Groundwater* 54: 171-185.

623

624 Illman W.A., X. Liu, S. Takeuchi, T.-C.J. Yeh, K. Ando, H. Saegusa. 2009. Hydraulic
625 tomography in fractured granite: Mizunami Underground Research site, Japan. *Water*
626 *Resources Research* 45: W01406.

627

628 Illman W.A., J. Zhu, A.J. Craig, D. Yin. 2010. Comparison of aquifer characterization
629 approaches through steady state groundwater model validation: A controlled laboratory
630 sandbox study. *Water Resources Research* 46: W04502.

631

632 Jardani A., J.P. Dupont, A. Revil, N. Massei, M. Fournier, B. Laignel. 2012. Geostatistical
633 inverse modeling of the transmissivity field of a heterogeneous alluvial aquifer under tidal
634 influence. *Journal of Hydrology* 472-473: 287-300.

635

636 Lavenue M., G. de Marsily. 2001. Three-dimensional interference test interpretation in a
637 fractured aquifer using the pilot point inverse method. *Water Resources Research* 37: 2659-
638 2675.

639

640 Le Borgne T., O. Bour, J.R. de Dreuzy, P. Davy, F. Touchard. 2004. Equivalent mean flow
641 models for fractured aquifers: Insights from a pumping tests scaling interpretation. *Water*
642 *Resources Research* 40: W03512.

643

644 Li W., A. Englert, O.A. Cirpka, H. Vereecken. 2008. Three-Dimensional Geostatistical
645 Inversion of Flowmeter and Pumping Test Data. *Ground Water* 46: 193-201.

646

647 Neuman S.P., P.A. Witherspoon. 1972. Field Determination of the Hydraulic Properties of
648 Leaky Multiple Aquifer System. *Water Resources Research* 8: 1284-1298.

649

650 Rabinovich A., W. Barrash, M. Cardiff, D.L. Hochstetler, T. Bakhos, G. Dagan, P.K. Kitanidis.
651 2015. Frequency dependent hydraulic properties estimated from oscillatory pumping tests in an
652 unconfined aquifer. *Journal of Hydrology* 531: 2-16.

653

654 Rasmussen T.C., K.G. Haborak, M.H. Young. 2003. Estimating aquifer hydraulic properties
655 using sinusoidal pumping tests in an unconfined aquifer. *Journal of Hydrology* 531: 2-16.

656

657 Sanchez-Vila X., P.M. Meier, J. Carrera. 1999. Pumping tests in heterogeneous aquifers: An
658 analytical study of what can be obtained from their interpretation using Jacob's method. *Water*
659 *Resources Research* 35: 943-952.

660

661 Sun A.Y., J. Lu, S. Hovorka. 2015. A harmonic pulse testing method for leakage detection in
662 deep subsurface storage formations. *Water Resources Research* 51: 4263-4281.

663

664 Wagner B.J. 1992. Simultaneous parameter estimation and contaminant source characterization
665 for coupled groundwater flow and contaminant transport modelling. *Journal of Hydrology* 135:
666 275-303.

667

668 Wen J.-C., C.-M. Wu, T.-C.J. Yeh, C.-M. Tseng. 2010. Estimation of effective aquifer
669 hydraulic properties from an aquifer test with multi-well observations (Taiwan). *Hydrogeology*
670 *Journal* 18: 1143-1155.

671

672 Yeh T.-C.J., S. Liu. 2000. Hydraulic tomography: Development of a new aquifer test method.
673 *Water Resources Research* 36: 2095-2105.

674

675 Yeh T.-C.J., C.-H. Lee. 2007. Time to change the way we collect and analyze data for aquifer
676 characterization. *Ground Water* 45: 116-118.

677

678 Zhou Y., D. Lim, F. Cupola, M. Cardiff. 2016. Aquifer imaging with pressure waves -
679 Evaluation of low-impact characterization through sandbox experiments. *Water Resources*
680 *Research* 52: 2141-2156.

681

682 Zhou Y., M. Cardiff. 2017. Oscillatory hydraulic testing as a strategy for NAPL source zone
683 monitoring: Laboratory experiments. *Journal of Contaminant Hydrology* 200: 24-34.

684

685 Zhu J., T.-C.J. Yeh. 2005. Characterization of aquifer heterogeneity using transient hydraulic
686 tomography. *Water Resources Research* 41: W07028.

687